論文 / 著書情報
Article / Book Information

Title	Performance of a geosynthetic cementitious composite mat for stabilising sandy slopes
Authors	Tan Phong Ngo, Suched Likitlersuang, Akihiro Takahashi
Citation	Geosynthetics International, Vol. 26, Issue 3, pp. 309-319
Pub. date	2019, 6
DOI	http://dx.doi.org/10.1680/jgein.19.00020
Note	This file is author (final) version.
Note	(c) Geosynthetics International, Vol. 26, Issue 3, pp. 309-319. This AAM is provided for your own personal use only. It may not be used for resale, reprinting, systematic distribution, emailing, or for any other commercial purpose without the permission of the publisher ’

Performance of a geosynthetic cementitious composite mat for stabilising sandy slopes

Tan Phong Ngo[1,2], Suched Likitlersuang[3] and Akihiro Takahashi[4]

[1] Former PhD student, Department of Civil Engineering, Faculty of Engineering, Chulalongkorn University, Bangkok, Thailand
[2] Lecturer, Department of Geotechnics, Faculty of Geology and Petroleum Engineering, Ho Chi Minh City University of Technology, VNU-HCM, Ho Chi Minh, Vietnam, E-mail: ngotanphong@hcmut.edu.vn
[3] Professor, Centre of Excellence in Geotechnical and Geoenvironmental Engineering, Department of Civil Engineering, Faculty of Engineering, Chulalongkorn University, Bangkok, Thailand, E-mail: fceslk@eng.chula.ac.th (corresponding author)
[4] Professor, Department of Civil and Environmental Engineering, Tokyo Institute of Technology, Tokyo, Japan, E-mail: takahashi.a.al@m.titech.ac.jp

ABSTRACT: In recent years, there has been much research interest in soil erosion and slope failure due to seepage and rainfall, especially toward finding new technologies/materials with which to stabilise soil slopes. Many geosynthetic materials have been developed to stabilise soil slopes while also being environmentally friendly and convenient for construction. In this study, the performance of a novel geosynthetic cementitious composite mat (GCCM) is studied regarding its ability to stabilise soil slopes. Physical model tests are performed on sandy soil slopes under seepage conditions both with and without GCCM stabilisation. Particle image velocimetry is used to measure the soil displacement, and standpipe piezometers are used to monitor the pore water pressure of the slope. The results show that the slope displacement with GCCM stabilisation is much smaller than that without it. The presence of the GCCM constrains the displacement near the slope surface to being along the slope, whereas without the GCCM the slope can deform freely especially in the middle to upper zone of slope area. The results indicate that the GCCM performs well at slope stabilisation.

Geosynthetics International, 26(3), 309-319, 2019

Original URL:

https://doi.org/10.1680/jgein.19.00020

NOTATION

c'	soil cohesion (kPa)
C_c	coefficient of curvature
C_u	coefficient of uniformity
D	depth of failure zone (mm)
D_{10}	10% of the particles are finer than this size (mm)
D_{30}	30% of the particles are finer than this size (mm)
D_{60}	60% of the particles are finer than this size (mm)
ϕ	angle of internal friction (^{o})
γ_d	dry unit weight (kN/m^3)
G_s	specific gravity
γ_{sat}	saturated unit weight (kN/m^3)
h_A	water pressure head at point A (mm)
h_B	water pressure head at point B (mm)
h_C	water pressure head at point C (mm)
h_D	water pressure head at point D (mm)
h_f	pressure head when the slope failed (mm)
h_m	pressure head when the slope started moving (mm)
k_{sat}	hydraulic conductivity (m/s)
L	length of failure zone (m)
SP	poorly graded sand
w/W_{GCCM}	ratio of water to dry mass of GCCM

KEYWORDS: Geosynthetic, Composite materials, Slope stabilisation, 1G physical model, Particle image velocimetry, Deformation

1. INTRODUCTION

Shallow slope failure is a geotechnical phenomenon related to the movement of soil at depths of less than 1.2 m (Evans 1972). While not causing major damage or loss of life, shallow slope failures can pose a hazard to infrastructure by damaging guardrails, shoulders, road surfaces and drainage facilities, for example, and they can affect traffic because of debris flows onto roads (Titi and Helwany 2007). However, if a shallow slope failure intersects an existing stream or channel, then it can cause a debris flow with the potential to do much damage to both life and property (Lee and Winter 2019). Shallow slope failures usually occur in the rainy season, with the seepage that develops parallel to the slope face due to rainfall being one of the main causes of slope instability (Day and Axten 1989; Muntohar and Liao 2010).

There has been much use of physical model tests to study slope stability in the presence of seepage flow. By measuring the pore water pressure, moisture content and slope deformation in a model sandy slope subjected to water percolation from the upslope, Orense *et al.* (2004) found that slope failure was always induced when the soil near the toe of the slope became nearly fully saturated; this finding was supported by observations made by Huang *et al.* (2009). In addition, there has been research into the use of geosynthetic materials for slope stabilisation. Almost three decades ago, geotextiles (Fowler and Koerner 1987) and geocell materials (Bush *et al.* 1990) were studied for constructing embankments on soft soil. Subsequently, many geosynthetic materials have been developed and applied for slope stabilisation and land reclamation, examples being three-dimensional polyethylene geocell material (Wu and Austin 1992), heavy-duty polyester woven geotextile (Raymond et al. 1993), geosynthetic mulch mats (Ahn *et al.* 2002), slurry-filled geotextile mats (Yan and Chu 2010) and biological geotextiles (Guerra *et al.* 2015). In addition, Thusyanthan *et al.* (2007) and Wang *et al.* (2011) studied geosynthetically reinforced soil slopes subjected to earthquake loads. For slope failure due to seepage flow, Rajabian *et al.* (2012) and Rajabian and Viswanadham (2016) conducted centrifuge model studies on fine sandy slopes under seepage conditions to evaluate the slope-stabilisation performance of anchored geosynthetic systems, and Akay *et al.* (2013) introduced a lightweight expanded-polystyrene geofoam for slope remediation.

Various techniques have been used to protect slopes from shallow failure, examples being vegetation (Wu 1994), live poles (Mafian *et al.* 2009; Wu *et al.* 2014), shotcrete (US-Army-Corps-of-Engineers 1995) and geosynthetic clay liners (GCLs) (Daniel *et al.* 1998; Gilbert and Wright 2010), but each has certain limitations. For example, (i) vegetation and live poles take time to grow and must be maintained regularly, (ii) the cover of shotcrete is not

always uniform in terms of quality and thickness and (iii) clay leakage can reduce the friction between GCLs and soil slopes (Bouazza 2002).

Recently, a geosynthetic cementitious composite mat (GCCM) made of geotextiles and cement powder was introduced (Jongvivatsakul et al. 2018; Jirawattanasomkul *et al.* 2018 and 2019). GCCMs have many attractive properties, examples being high strength and stiffness after setting, uniform thickness and the fact that they are simple to install in the field. Therefore, GCCMs could be used for slope stabilisation, erosion control, containment and ditch lining. In addition, in early 2018 a new standard guide was released for the site preparation, layout, installation and hydration of GCCMs (ASTM-D8173-18), an event that represents a milestone in promoting and developing GCCMs, especially for geotechnical engineering applications.

To study the performance of a stabilised slope, it is crucial to be able to measure the extent of any slope deformation. Various image-based analysis techniques are used to measure the planar deformation of soil in geotechnical tests, examples being X-rays (Arthur *et al.* 1964; Roscoe *et al.* 1963), stereo photogrammetry (Andrawes and Butterfield 1973; Butterfield *et al.* 1970) and particle image velocimetry (PIV) (Paikowsky and Xi 2000; Taylor *et al.* 1998; White *et al.* 2003). Of these, PIV is an important technique for measuring velocities in fluid dynamics (Adrian 1991), allowing the instantaneous measurement of the velocity (and related properties) in a specific area (known as the interrogation area) in the fluid. PIV arose from laser speckle velocimetry, which was developed in the late 1970s (Dainty 1975). In PIV, the displacement of the interrogation area between two digital images is calculated using cross-correlation or autocorrelation techniques. In the present study, PIV is used to measure the deformation of soil slopes because it is a relatively simple and inexpensive technique that does not require the use of target markers.

The aim of the present paper is to assess the potential for using GCCMs to stabilise sandy slopes in the presence of seepage flow. In physical model tests, the GCCM properties are evaluated and PIV is used to measure the slope displacement.

2. MATERIALS

2.1. Geosynthetic cementitious composite mat (GCCM)

A GCCM is a manufactured product comprising two geotextile layers and a dry cement layer bound together with needle punching as shown in Figure 1(a). The present final product is a 10-mm-thick and 1-m-wide GCCM roll can be produced up to a maximum length of 30 m as shown in Figure 1(b). Because the GCCM is manufactured in a factory, its properties are more

uniform than those of a product that is installed in the field, such as shotcrete. After water spraying, the cement hydration that takes place in the GCCM turns it into a solid mat with high stiffness and tensile strength. In addition, the presence of the geotextile layers at the top and bottom of the GCCM helps it to absorb large strains due to external loads in practice. Moreover, the GCCM can be installed relatively simply and quickly for slope stabilisation; it is simply laid on the slope surface and then sprayed with water [Figure 1(c)]. Given the aforementioned advanced characteristics, the GCCM has many potential geotechnical applications, such as slope protection, erosion control, ditch lining and water containment as hydraulic barriers (ASTM-D8173-18).

Table 1 summarises the basic physical and mechanical properties of the GCCM after a curing time of 7 d, namely its mass per unit area (ASTM-D5993-14), nominal thickness (ASTM-D5199-06), tensile strength (ASTM-D6768), bending strength (BS-EN-12467), puncture resistance (ISO-12236) and water permeability (BS-EN-12467). The ratio of water to dry mass (w/W_{GCCM}) of the GCCM is 0.5, and curing is done by soaking under ambient laboratory conditions. More details of these tests can be found in Jongvivatsakul *et al.* (2018).

The GCCM interfacial resistance is proportional to the interfacial friction between the GCCM and the soil, and therefore the latter is an important property, especially in slope stabilisation. The interfacial friction angle between the GCCM and sand used in the present physical model tests as determined by direct shear tests (ASTM-D3080-98) with a normal stress of 7–50 kPa is 36°, as shown in Figure 2.

2.2. Sand

The specimen soil used in the present physical model tests is fine yellow sand taken from a river bank around 80 km north of Bangkok, Thailand. According to the Unified Soil Classification System (USCS), the sand is classified as poorly graded sand (SP). The particle size distribution as determined by sieving according to ASTM D422 is shown in Figure 3, where it can be seen that the specimen sand is uniformly graded with a particle size that varies in the relatively narrow range of 0.106–0.425 mm. The sand is cohesionless, and Figure 2 shows that the internal friction angle based on a direct shear test according to ASTM D3080 is 38°. The average hydraulic conductivity of the saturated sand with a dry unit weight of 14.2–14.7 kN/m^3 at 29°C (i.e. the ambient laboratory temperature) as determined by the constant-water-head method according to ASTM D2434 is 2.1×10^{-4} m/s, as shown in Figure 4. The

results show that the hydraulic conductivity is inversely proportional to the dry unit weight, and the sand properties are summarised in Table 2.

3. CALIBRATION OF PARTICLE IMAGE VELOCIMETRY

The displacement of the soil slope is measured using the open-source PIV analysis software OpenPIV, which is written in MATLAB and was developed by Taylor *et al.* (2010). The size of the selected interrogation area is 128×128 pixels, equivalent to 4.5 cm × 4.5 cm in the prototype. Note that because OpenPIV outputs the horizontal and vertical velocities of soil particle, the soil displacement is then calculated by accumulation of two such velocity components multiplied by time.

To evaluate the accuracy and precision of the PIV technique, a series of calibration tests is conducted using an acrylic calibration tool as shown in Figure 5. The calibration tool comprises an upper box and a lower box, the former being free to slide on the latter. A screw and a dial gauge are used to control and measure the horizontal movement of the upper box, as shown in Figure 5. A sliding guide located on the surface of the lower box ensures that the upper box moves only horizontally, and a steel ruler is attached to the lower box as a reference. The calibration is conducted using the same sand intended to use in the physical model test but with a saturation degree (i.e. water content) ranging from zero to 90%. A high-resolution camera with a resolution of 18 megapixels and a frame rate of 5 frame per second is used in this study. The calibration is conducted carefully in a 3.0-m-long, 2.0-m-wide and 2.0-m-high chamber with lighting provided by two LED spotlights.

The upper box of sand is translated using the screw bolt attached on the right side of the lower box, and a photograph is taken after each 1 mm of translation. Here, accuracy is defined as the systematic difference between the PIV-measured value and the true value read from the dial gauge, whereas precision is defined as the random difference among multiple measurements of the same quantity, i.e. the standard error. The calibration results in Figure 6 show that for the 128×128-pixel patch, the PIV measurements have an average accuracy of 0.13 mm (equivalently to 2.6 pixels) and a precision of 0.005 mm (equivalently to 0.01 pixels). Note that the image distortion is neglected in the analysis. Alternatively, expressing the accuracy as a fraction of the field of view (FOV) width (i.e. by dividing the accuracy in pixels by the image width in pixels, 4,608 pixels), the present accuracy is 1/1,772, which is clearly better than the accuracy of 1/1,266 achieved by (Paikowsky and Xi 2000).

4. PHYSICAL MODEL

4.1. Slope model

A 2.0-m-long, 1.2-m-high and 0.2-m-wide acrylic tank as shown in Figure 7 is constructed and used for the physical model tests of the soil slope. Each 10-mm-thick side of the tank is transparent, which is useful for monitoring and photographing the soil slope during the tests. The model slope is constructed in the 1.5-m-long middle section, while the remaining sections on the left and right are used as chambers for water supply and drainage, respectively. The water chambers and the soil model are separated by perforated stainless-steel walls covered with stainless-steel wire mesh with opening holes of 0.1 mm to allow water move through without washing out the soil particles. Each water chamber is connected to a water supply tank to maintain a constant water head; to ensure a stable and continuous water supply, an electric pump with a capacity of 5 L/min is used to supply water during the tests. To measure the water pressure head in the soil, two 6-mm-diameter standpipes are installed along the base of the soil slope at the locations shown in Figure 7.

The 1.5-m-long, 0.3-m-deep and 0.2-m-wide model sandy slope is built on an impermeable base inclined at 33° and a 0.15 m flat base near the slope toe. The front and rear inner surfaces of the tank are coated with petroleum jelly to reduce the friction between the soil slope and the tank sides. The interfacial friction angle between the sand and the acrylic is measured both with and without the petroleum jelly; it is 16.7° with the petroleum jelly and 19.5° without it. Therefore, the slope model can be simplified as plane strain condition. A mixture of silicon glue and sand particles of size 1–2 mm is applied to the top surface of the impermeable base to form a rough base.

Each homogenous model sandy slope is constructed with a dry unit weight of approximately 14.5 kN/m^3. The sand is first dried in air and then used to construct the model slope. To obtain a uniform slope and consistent and repeatable specimen preparation, the slope ground is divided into four layers for compaction, each of which is compacted gently with a tamping rod to obtain the target height.

A camera is positioned 2 m in front of the tank to photograph the slope every 30 s during the tests, and two steel rulers are attached to the front surface of the tank as references. Note that the accuracy of the PIV technique used to measure the soil displacement in this study is 0.13 mm as mentioned in Section 3, and the duration of each test is approximately 20 min.

4.2. Experimental program

Two experiments are carried out under the condition of seepage flow, namely one in which the slope is not stabilised slope (case 1) and one in which the slope is stabilised by a GCCM (case 2). In case 2, a 1.7-m-long and 0.19-m-wide GCCM that has been cured for 7 d is placed directly on the slope surface. To avoid any friction between the GCCM and the acrylic, a gap of 5 mm is provided on each side of the GCCM to prevent it from interacting with the tank sides, which could affect the test results. Moreover, there is a 50 mm gap between the GCCM and the steel mesh located at the toe to prevent them from coming into contact. Note that the interfacial friction between the GCCM and the sand prevents the former from sliding off the slope surface.

4.3. Test procedure

In many cases, a shallow slope can destabilise when subjected to seepage flow, therefore the aim here is to model a real slope with rising groundwater. The test procedure comprises two stages, namely saturation and seepage flow. Before conducting a test, the lower part of the sandy slope, namely the zone located near the impermeable base, is saturated by applying a constant water pressure head (h_A) of 130 mm at the upslope; to keep h_A constant, there is a series of 10 mm diameter holes in the right-hand side of the supply chamber to control the water level (see Figure 7). To control h_A, only one 10 mm diameter hole at the target water level was opened while the other were closed. The seepage flow reaches the toe of the slope after approximately 1 h, whereupon it takes roughly the same time again for the water pressure head at the toe of the slope (h_D) to reach the target value of 200 m. To allow the seepage flow to stabilise, h_A and h_D are then maintained for 30 min, during which time the outlet flow rate is monitored. Note that h_D remains constant at 200 mm during the test.

Upon saturation, an electric pump delivers water to the supply chamber to raise h_A gradually from 0.13 m. The blue lines in Figure 8 show that on average the water in case 1 (not stabilised) rises slightly more slowly than it does in case 2 (stabilised). During each test, care is taken to avoid disturbing either the physical model or the lighting conditions, which would affect the quality of the photographs taken for PIV analysis. Each test is terminated when either the slope collapses or h_A reaches the maximum level of 250 mm (i.e. to avoid an overflow).

5. RESULTS

All the results presented here arise from the information contained in the photographs taken during the tests. The pressure heads are determined from the standpipes and the water levels in the chambers at either end of the model slope, and the soil displacement is measured using PIV.

5.1. Water pressure heads

The water pressure heads at positions A–D (i.e. the supply chamber, standpipes 1 and 2 and the drainage chamber, respectively, as shown in the inset of Figure 8) are determined from each photograph taken, thereby recording how the water pressure heads change with time, as shown in Figure 8. In both cases 1 and 2, h_B and h_C clearly increase as h_A is increased. However, because soil wetting is required before the water level in the slope can rise, the rises in h_B and h_C are delayed relative to that in h_A.

In case 1, at the elapsed time of 7 min (i.e. when h_A reaches 186 mm), the crest of the slope is seen to move [as shown in Figure 13(a)]. It is also interesting to note that h_B starts increasing rapidly half a minute later (i.e. at the elapsed time of 7.5 min) despite h_A still being increased gradually. This observation suggests that the slope movement plays a role in the increase of h_B. In case 2 by contrast, the slope crest does not move until the elapsed time of 15 min, and h_B increases gradually throughout the entire test.

5.2. Soil displacement

To interpret how the soil slope deforms, eight vertical and 13 oblique cross sections are considered as shown in Figure 9, the spacing between them being 180 mm and 22 mm, respectively. Noted that vertical cross section V3 is considered in Figure 10 because the PIV observations show that the displacement is highest there, making it likely to be the location of greatest instability. This also confirmed by a plot of the deformation at V3 generated by water pressure variation at the point A (Figure 12).

Figure 10 shows the soil displacement versus h_A at V3 at the depths of 22, 66, 110, 154, 198, 242 and 286 mm. The soil displacement clearly increases with h_A, with the maximum soil displacement being 45 mm and 7 mm in cases 1 and 2, respectively. The considerably reduced displacement in case 2 indicates that the GCCM helps reduce the slope deformation.

In case 1, the slope displacement becomes rapid when h_A reaches 213 mm (approximately 71% of the depth of the model slope), as shown in Figure 10(a). In case 2 by contrast, the slope displacement remains gradual when h_A reaches 213 mm and even as high as

246 mm, as shown Figure 10(b). This shows that the GCCM contributes to the slope resistance and decreases the deformation. The soil displacement at the other vertical cross sections is similar to that at V3 but with smaller magnitude. At each vertical cross section, there is very little soil movement at the depth of 286 mm, which is due to the roughness of the base.

Figure 11 shows the typical shape of the curve of displacement versus water pressure head at shallower depth, in which there are two points of sudden change (denoted as P_m and P_f). The pressure heads at P_m and P_f (denoted as h_m and h_f, respectively) are interpreted as those when the slope starts to move and fails, respectively, thereby allowing them to be determined as $h_m = 186$ mm and $h_f = 213$ mm in case 1 and $h_m = 230$ mm in case 2 (h_f cannot be determined because the slope does not fail).

To interpret how the slope displacement varies with depth, the former is re-plotted as shown in Figure 12. In case 1 [i.e., no stabilisation; Figure 12(a)], when h_A is relatively small (i.e. $h_A = 186$ mm), the soil movement is zero at the base and increases fairly steadily toward the slope surface; it drops slightly in the shallowest zone where the soil is above the water table. However, when h_A is relatively high ($h_A = 216$ mm), the slope begins to collapse and there is much more soil movement. In case 2 by contrast [i.e. with GCCM stabilisation; Figure 12(b)], the soil displacement is zero at the base, increases to a pronounced maximum at a certain depth and then decreases toward the surface. The maximum displacements near the surface in case 1 and 2 for $h_A = 216$ mm are 44 mm and less than 5 mm, respectively, which at approximately eightfold is a relatively large difference. In case 2 with GCCM stabilisation, existence of the mat could contribute to equalisation of the soil movement near the surface. On the other hand, in case 1 no stabilisation, the failure starts from the highest movement layer and propagates toward the upslope.

The directions in which the soil slope moves can be presented in terms of the velocity vectors of the soil particles as derived from OpenPIV, as shown in Figure 13. The results indicate that the major direction of movement is nearly parallel to the base of the slope. In addition, the failure zone can be detected from the velocity vectors, as shown in Figure 13(b). The depth of the failure zone varies from section to section and tends to be deeper at the upslope and shallower at the downslope. The maximum depth (D) and length (L) of the failure zone are approximately 0.1 m and 1.7 m, respectively, which at $D/L \approx 6\%$ means that the failure can be classified as a translational failure according to Abramson *et al.* (2002) and Hansen (1984).

The soil slope is photographed after each test, as shown in Figure 14. The non-stabilised slope has failed absolutely after the test, but the GCCM-stabilised slope remains stable.

6. DISCUSSION

The increased pore water pressure and hydraulic force due to the seepage flow cause the slope displacement and failure. The soil is displaced throughout the slope by different amounts, with those at shallow depth and at the upslope being the greatest. The slope deformation due to seepage flow comprises the stable stage, the moving stage and the failure stage, the transitions between which correspond to points P_m and P_f of sudden change. This implies that slope failure might be preceded by some warning signs, namely those associated with the moving stage. For example, a landslide occurred in the city of Antipolo in the Philippines in August 1999, burying many houses; however, according to Punongbayan R et al. (2002), there had been warning signs (e.g. cracks forming in the walls of houses) several months earlier. In addition, Voight (1989), Crosta and Agliardi (2003) and Sasahara (2017) have discussed soil displacement as a precursor of creep failure.

In the mechanism for GCCM stabilisation, the stiffness of the GCCM is a key factor. The downslope constraint (i.e. the retaining wall at the downslope) means that in the tests the slope deformation occurs between the midslope and the upslope. Given that (i) the GCCM is much stiffer than the soil and (ii) the GCCM–soil interfacial friction is comparable to the internal soil friction, as shown in Section 5, the effect of the GCCM is to equalize the along-slope displacement near the slope surface. Consequently, a relatively large deformation occurs in the midslope in case 1, whereas the surface displacement is smaller in case 2 because of the displacement-equalisation function of the GCCM. Moreover, the weight of the GCCM acting on the slope increases the effective stress, thereby increasing the stability of the GCCM-stabilised slope.

During a test, the PIV technique gives the magnitude and direction of the soil displacement at any location and time with an accuracy of 0.13 mm, from which the failure surface can be defined. Note that the PIV technique requires no markers to be placed within the model slope and thus does not disturb its behaviour, unlike if the displacement is measured using a tiltmeter or accelerometer as an inclinometer (Orense *et al.* 2004; Sasahara 2017); burying sensors inside the model slope may affect the soil movement (Zhang *et al.* 2009). It should be emphasised that PIV measures only the soil deformation at the side of the tank facing the camera, and therefore the relatively high friction between the soil and the tank could affect the soil deformation, which is why petroleum jelly is applied there.

7. CONCLUSIONS AND RECOMMENDATIONS

Physical model tests of a sandy slope with and without a GCCM were performed under seepage conditions, and the PIV technique worked well for measuring the slope deformation. In the present study, the PIV accuracy was 0.13 mm, which is less than the effective diameter (D_{10} = 0.16 mm) of the sand grains. The results show that the GCCM stabilised the slope by means of displacement equalisation and applying a frictional force and a normal force to the slope surface. Consequently, the deformation of the slope stabilised with the GCCM was significantly smaller than that of the one with no GCCM.

In the present study, the GCCM performed well at reinforcing the sandy slope in the presence of seepage flow. However, the effectiveness of GCCM stabilisation for slopes of other types of soils (e.g. silt, sandy clay, clay etc.) and other conditions (e.g. seepage, rainfall etc.) is yet to be studied. These issues should be investigated and evaluated in future work involving physical models, centrifuge models, numerical simulations and/or field studies.

ACKNOWLEDGEMENTS

This research was supported by the Thailand Research Fund (grant no. DBG-6180004) and the Ratchadapisek Sompoch Endowment Fund (2019) of Chulalongkorn University (grant no. 762003-CC). The authors would like to thank the Siam Cement Group (SCG) for providing some of the materials used in the tests. The first author wishes to thank the AUN/SEED-Net (JICA) for a scholarship during his PhD study at Chulalongkorn University. The second author would like to acknowledge the travel grant from Chulalongkorn University in support of his visiting scholarship at the Tokyo Institute of Technology in 2017.

REFERENCES

Abramson, L., Lee, T., Sharma, S. & Boyce, G. (2002). *Slope Stability and Stabilization Methods*, John Wiley, New York.

Adrian, R. J. (1991). Particle-Imaging techniques for experimental fluid mechanics. *Annual Review of Fluid Mechanics*, **23**, 261–304.

Ahn, T. B., Cho, S. D. & Yang, S. C. (2002). Stabilization of soil slope using geosynthetic mulching mat. *Geotextiles and Geomembranes*, **20**, No. 2, 135–146.

Akay, O., Özer, A. T., Fox, G. A., Bartlett, S. F. & Arellano, D. (2013). Behavior of sandy slopes remediated by EPS-block geofoam under seepage flow. *Geotextiles and Geomembranes*, **37**, 81–98.

Andrawes, K. Z. & Butterfield, R. (1973). The measurement of planar displacements of sand grains. *Géotechnique*, **23**, No. 4, 571–576.

Arthur, J. R. F., James, R. G. & Roscoe, K. H. (1964). The determination of stress fields during plane of a sand mass. *Géotechnique*, **14**, No. 4, 283–308.

ASTM D3080-98. *Standard Test Method for Direct Shear Test of Soils Under Consolidated Drained Conditions*, ASTM International, West Conshohocken, PA, USA.

ASTM D5199-06. *Standard Test Method for Measuring the Nominal Thickness of Geosynthetics*, ASTM International, West Conshohocken, PA, USA.

ASTM D5993-14. *Standard Test Method for Measuring Mass Per Unit of Geosynthetic Clay Liners*, ASTM International, West Conshohocken, PA, USA.

ASTM D6768. *Standard Test Method for breaking force and elongation of textile fabrics*, ASTM International, West Conshohocken, PA, USA.

ASTM D8173-18. *Site Preparation, Layout, Installation, and Hydration of Geosynthetic Cementitious Composite Mats*, ASTM International, West Conshohocken, PA, USA.

Bouazza, A. (2002). Geosynthetic clay liners. *Geotextiles and Geomembranes*, **20**, No. 1, 3–17.

BS-EN-12467. *Fibre-cement flat sheets - Product specification and test methods*, BSI Standards Limited, European Committee For Standardization, Brussels.

Bush, D. I., Jenner, C. G. & Bassett, R. H. (1990). The design and construction of geocell foundation mattresses supporting embankments over soft grounds. *Geotextiles and Geomembranes*, **9**, No. 1, 83–98.

Butterfield, R., Harkness, R. M. & Andrews, K. Z. (1970). A stero-photogrammetric method for measuring displacement fields. *Géotechnique*, **20**, No. 3, 308–314.

Crosta, G. B. & Agliardi, F. (2003). Failure forecast for large rock slides by surface displacement measurements. *Canadian Geotechnical Journal*, **40**, No. 1, 176–191.

Dainty, J. C. (1975). *Laser Speckle and Related Phenomena*, Springer-Verlag Berlin Heidelberg.

Daniel, D. E., Koerner, R. M., Bonapart, R., Landreth, R. E., Carson, D. A. & Scranton, H. B. (1998). Slope stability of geosynthetic clay liner test plots. *Journal of Geotechnical and Geoenvironmental Engineering*, **124**, No. 7, 628–637.

Day, R. W. & Axten, G. W. (1989). Surficial stability of compacted clay slopes. *Journal of Geotechnical Engineering*, **115**, No. 4, 577–580.

Evans, D. A. (1972). *Slope Stability Report*, Slope Stability Committee, Department of Building and Safety, Los Angeles, CA.

Fowler, J. & Koerner, M. (1987). Stabilization of very soft soils using geosynthetics. *Proceedings of Geosynthetics '87*, 289–300.

Gilbert, R. B. & Wright, S. G. (2010). Slope stability with geosynthetic clay liners. *Geosynthetic Clay Liners for Waste Containment Facilities*, CRC Press, 169–202.

405 Guerra, A. J. T., Bezerra, J. F. R., Fullen, M. A., Mendonça, J. K. S. & Jorge, M. C. O. (2015).
406 The effects of biological geotextiles on gully stabilization in São Luís, Brazil. *Natural*
407 *Hazards*, **75**, No. 3, 2625–2636.
408 Hansen, M. J. (1984). Strategies for classification of landslides. *Slope Instability* (eds. D.
409 Brunsden & D. B. Prior), Wiley, Chichester, 1–25.
410 Huang, C. C., Ju, Y. J., Hwu, L. K. & Lee, J. L. (2009). Internal soil moisture and piezometric
411 responses to rainfall-induced shallow slope failures. *Journal of Hydrology*, **370**, No. 1,
412 39–51.
413 ISO-12236. *Geosynthetic static puncture test*, Bureau of Indian Standards: India.
414 Jirawattanasomkul, T., Kongwang, N., Jongvivatsakul, P. and Likitlersuang, S. (2018). Finite
415 element modelling of flexural behaviour of Geosynthetic Cementitious Composite Mat
416 (GCCM). *Composites Part B: Engineering*, **154**, 33-42.
417 Jirawattanasomkul, T., Kongwang, N., Jongvivatsakul, P. and Likitlersuang, S. (2019). Finite
418 element analysis of tensile and puncture behaviours of geosynthetic cementitious
419 composite mat (GCCM). *Composites Part B: Engineering*, **165**, 702-711.
420 Jongvivatsakul, P., Ramdit, T., Ngo, T. P. & Likitlersuang, S. (2018). Experimental
421 investigation on mechanical properties of geosynthetic cementitious composite mat
422 (GCCM). *Construction and Building Materials*, **166**, 956–965.
423 Lee, S. G. & Winter, M. G. (2019). The effects of debris flow in the Republic of Korea and
424 some issues for successful risk reduction. *Engineering Geology*, in press.
425 Mafian, S., Huat, B. B. K., Rahman, N. A. & Singh, H. (2009). Potential plant species for live
426 pole application in tropical environment. *American Journal of Environmental Sciences*,
427 **5**, No. 6, 759–764.
428 Muntohar, A. S. & Liao, H. J. (2010). Rainfall infiltration: infinite slope model for landslides
429 triggering by rainstorm. *Natural Hazards*, **54**, No. 3, 967–984.
430 Orense, R., Shimoma, S., Maeda, K. & Towhata, I. (2004). Instrumented model slope failure
431 due to water seepage. *Journal of Natural Disaster Science*, **26**, No. 1, 15–26.
432 Paikowsky, S. & Xi, F. (2000). Particle motion tracking utilizing a high-resolution digital CCD
433 camera. *Geotechnical Testing Journal*, **23**, No. 1, 123–134.
434 Punongbayan R, S., Arboleda R, A., Bornas M, V. & Abigania M, T. (2002). The 3 August
435 1999 Cherry Hills Landslide in Antipolo City, Philippines. *Landslide News*, 13, 12-15.
436 Rajabian, A. & Viswanadham, B. V. S. (2016). Behaviour of anchored geosynthetic-reinforced
437 slopes subjected to seepage in a geotechnical centrifuge. *Geosynthetics International*,
438 **23**, No. 1, 36–47.
439 Rajabian, A., Viswanadham, B. V. S., Ghiassian, H. & Salehzadeh, H. (2012). Centrifuge
440 model studies on anchored geosynthetic slopes for coastal shore protection. *Geotextiles*
441 *and Geomembranes*, **34**, 144–157.
442 Raymond, G. P., Giroud, J. P., International Society of Soil, M., Foundation, E., Technical
443 Committee Tc, G. & Geosynthetics (1993). *Geosynthetics Case Histories*, International
444 Society for Soil Mechanics and Foundation Engineering; BiTech Publishers, [S.l.];
445 Richmond, B.C.
446 Roscoe, K. H., Arthur, J. R. F. & James, R. G. (1963). Determination of strains in soils by X-
447 ray method. *Civil Engineering and Public Works Review*, **58**, 873–876.
448 Sasahara, K. (2017). Prediction of the shear deformation of a sandy model slope generated by
449 rainfall based on the monitoring of the shear strain and the pore pressure in the slope.
450 *Engineering Geology*, **224**, 75–86.
451 Taylor, Z. J., Gurka, R., Kopp, G. A. & Liberzon, A. (2010). Long-duration time-resolved PIV
452 to study unsteady aerodynamics. *Instrumentation and Measurement*, **59**, No. 12, 3262–
453 3269.

454 Thusyanthan, N. I., Madabhushi, S. P. G. & Singh, S. (2007). Tension in geomembranes on
455 landfill slopes under static and earthquake loading—centrifuge study. *Geotextiles and*
456 *Geomembranes*, **25**, No. 2, 78–95.
457 Titi, H. & Helwany, S. (2007). Investigation of vertical members to resist surficial slope
458 instabilities, (WHRP 07–03). Wisconsin Department of Transportation, Madison, WI.
459 US-Army-Corps-of-Engineers (1995). *Standard Practice for Shotcrete*, American Society of
460 Civil Engineers, New York.
461 Voight, B. (1989). A relation to describe rate-dependent material failure. *Science*, **243**,
462 No. 4888, 200–203.
463 Wang, L., Zhang, G. & Zhang, J. M. (2011). Centrifuge modeling of failure behavior of pile-
464 reinforced slope. *Proceedings of the 14th Asian Regional Conference on Soil*
465 *Mechanics and Geotechnical Engineering*, 383-389
466 White, D. J., Take, W. A. & Bolton, M. D. (2003). Soil deformation measurement using particle
467 image velocimetry (PIV) and photogrammetry. *Géotechnique*, **53**, No. 7, 619–631.
468 Wu, K. J. & Austin, D. N. (1992). Three-dimensional polyethylene geocells for erosion control
469 and channel linings. *Geotextiles and Geomembranes*, **11**, No. 4, 611–620.
470 Wu, T. H. (1994). Slope stabilization using vegetation. *Geotechnical Engineering: Emerging*
471 *Trends in Design and Practice*, 377–403.
472 Wu, T. H., Kokesh, C. M., Trenner, B. R. & Fox, P. J. (2014). Use of live poles for stabilization
473 of a shallow slope failure. *Journal of Geotechnical and Geoenvironmental Engineering*,
474 **140**, No. 10, 05014001.
475 Yan, S. W. & Chu, J. (2010). Construction of an offshore dike using slurry filled geotextile
476 mats. *Geotextiles and Geomembranes*, **28**, No. 5, 422–433.
477 Zhang, G., Hu, Y. & Zhang, J. M. (2009). New image analysis-based displacement-
478 measurement system for geotechnical centrifuge modeling tests. *Measurement*, **42**,
479 No. 1, 87–96.

480 **List of Figures**

502

(a)

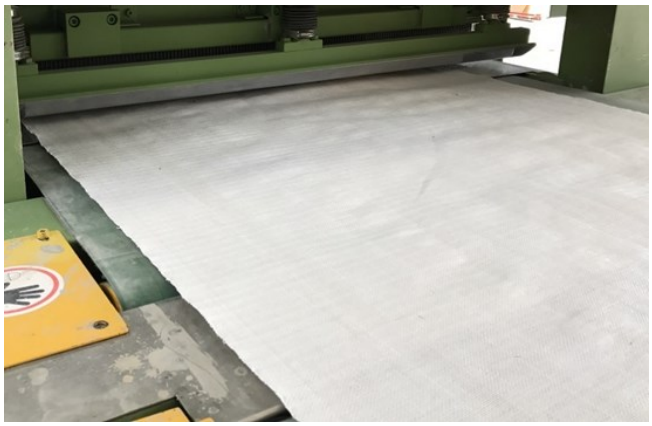

(b)

(c)

Figure 1. Typical geosynthetic cementitious composite mat (GCCM) and its application: (a) GCCM composition; (b) manufacturing process; (c) installation and water spraying of GCCM on slope surface.

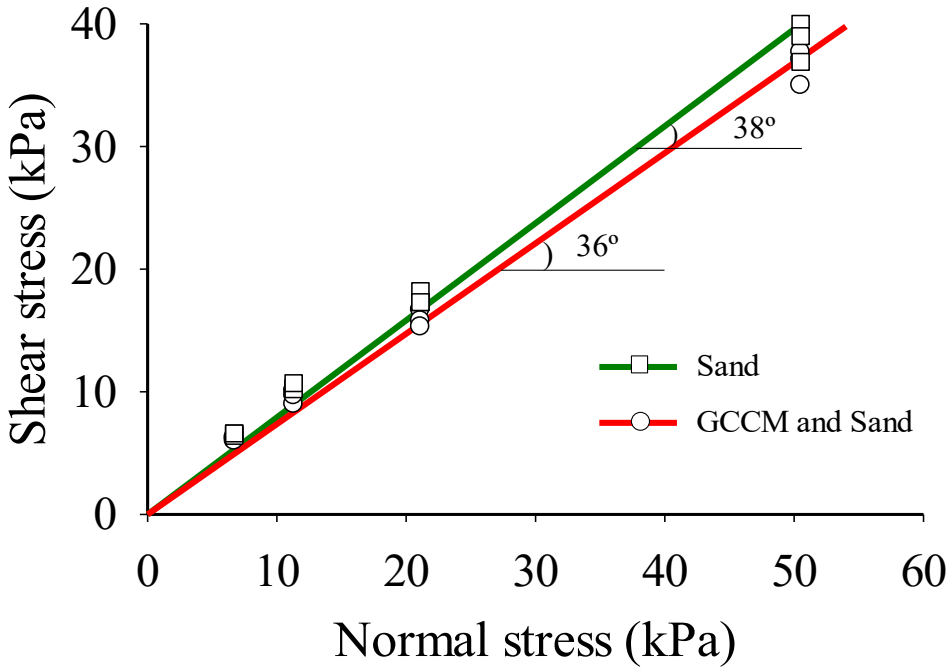

507

508 **Figure 2. Results of direct shear tests.**

509

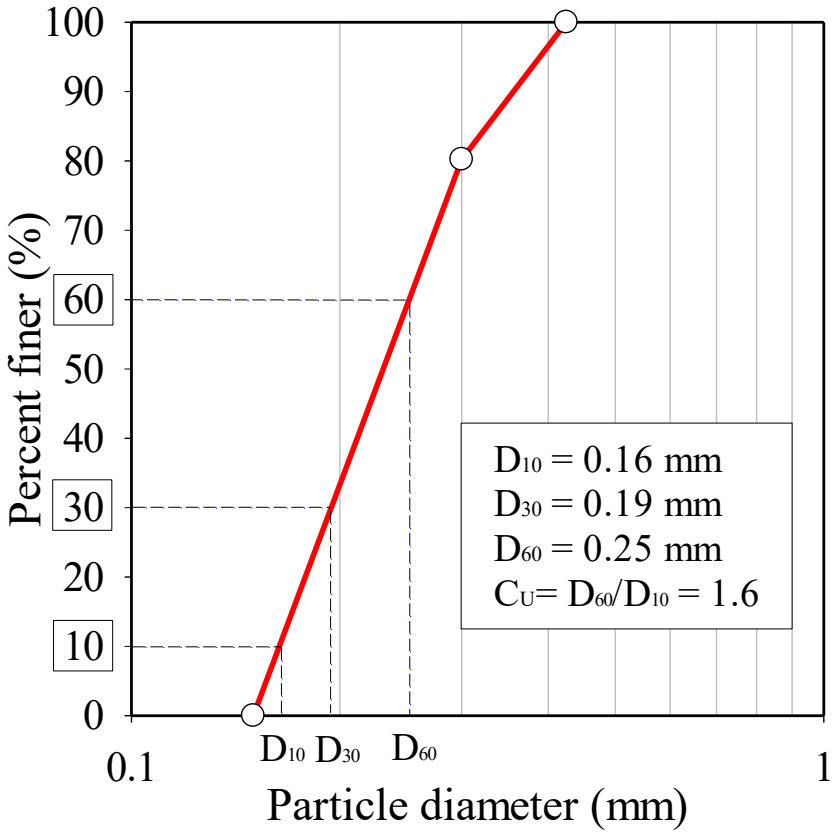

510

511 **Figure 3. Grain size distribution of sand.**

512

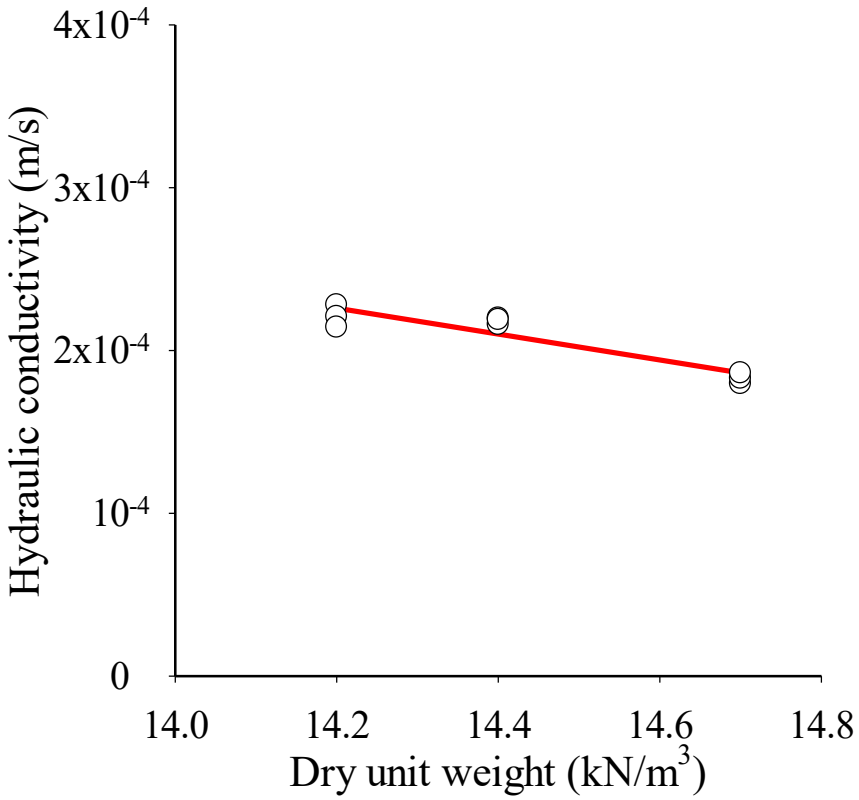

513

514 **Figure 4. Results of hydraulic conductivity test.**

515

516

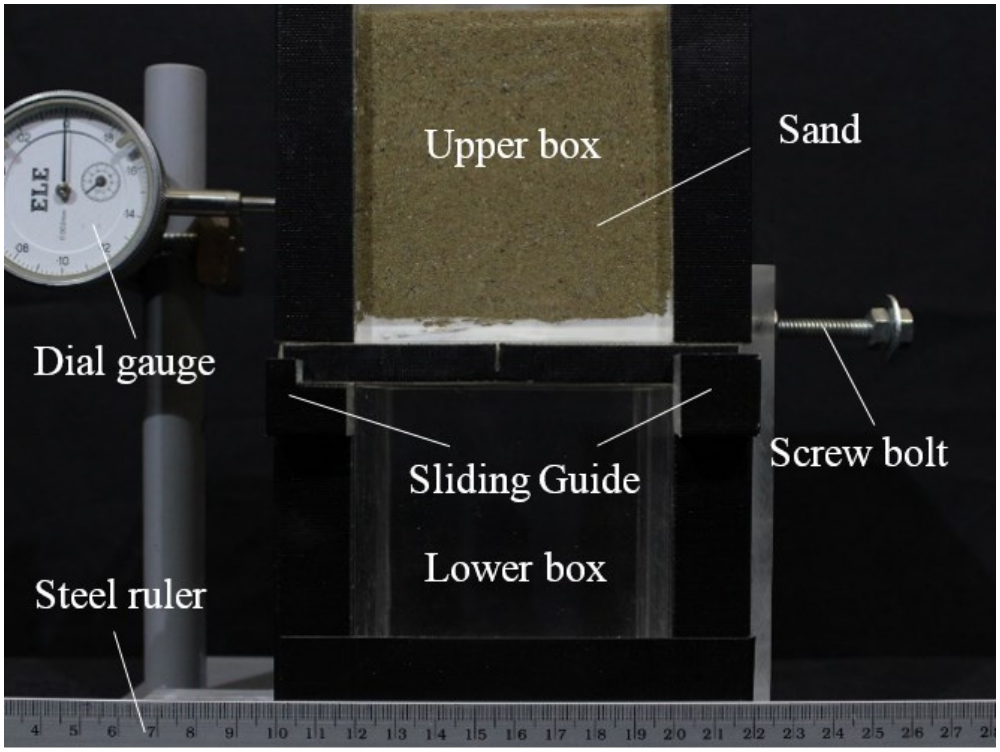

Figure 5. Calibration tool.

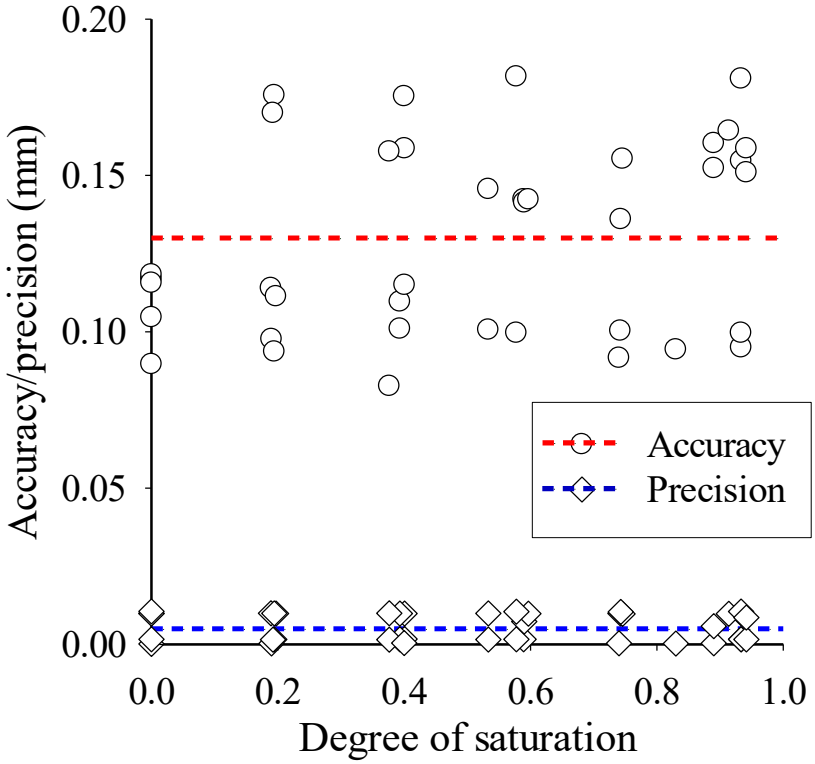

520

521 **Figure 6. Variation of accuracy and precision with saturation degree. Red and blue**

522 **dashed lines show average accuracy and precision, respectively.**

523

524

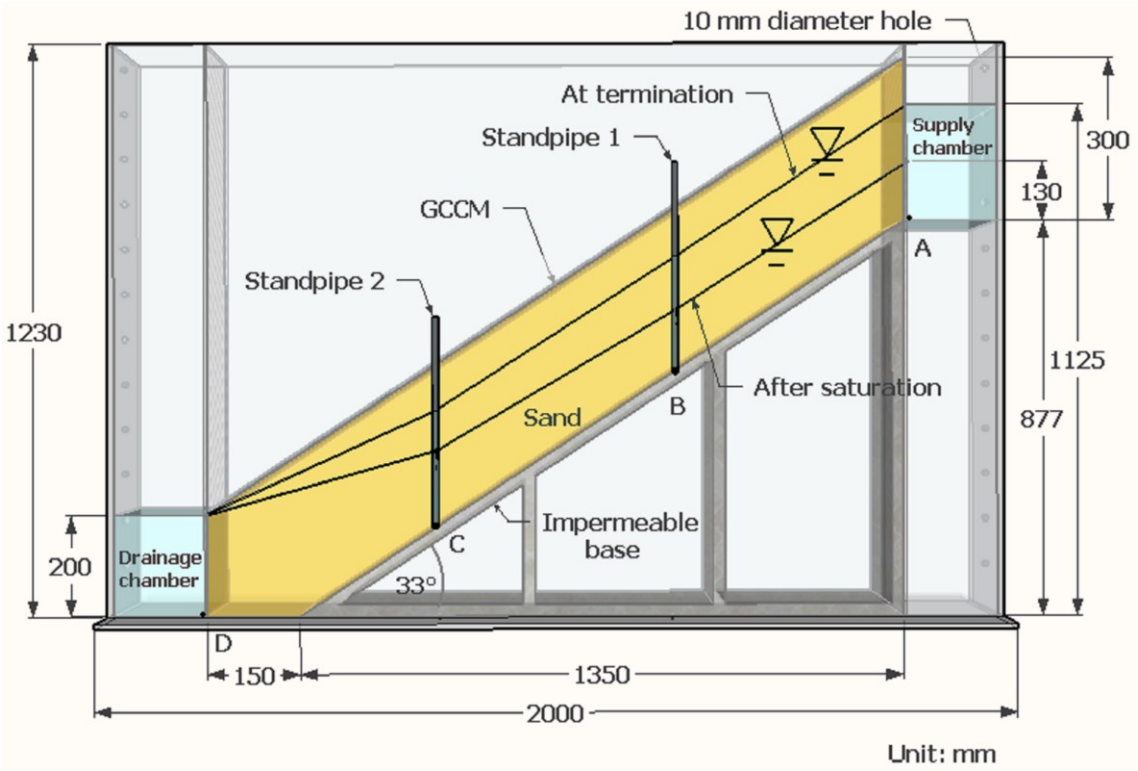

525

526 **Figure 7. Schematic of physical model.**

527

528

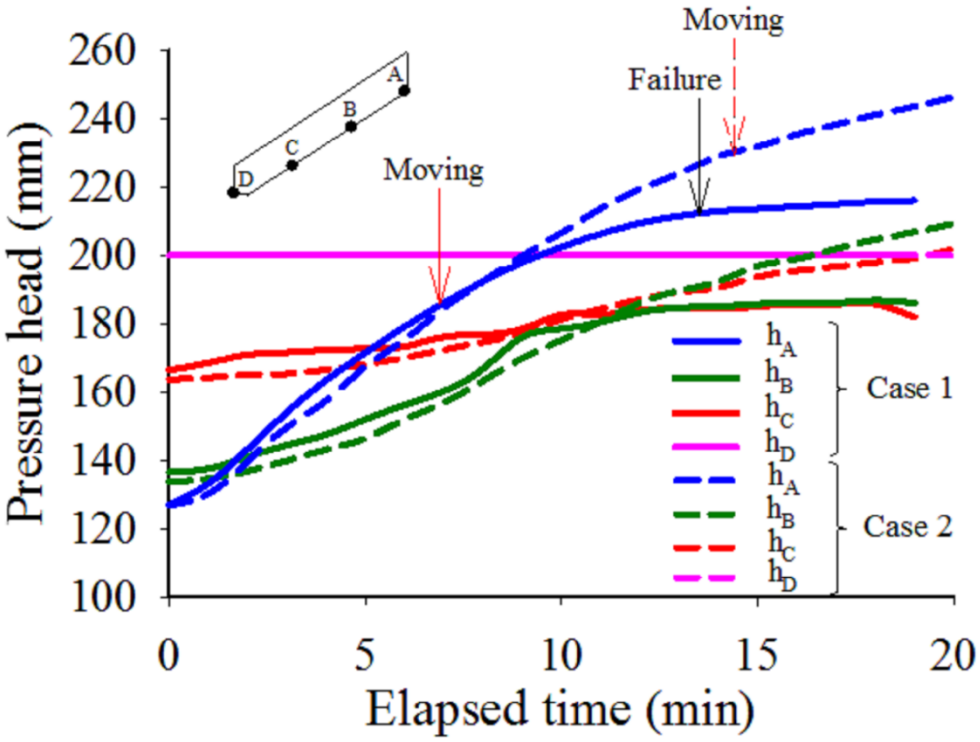

529

530 **Figure 8. Variations of water pressure heads with time.**

531

532

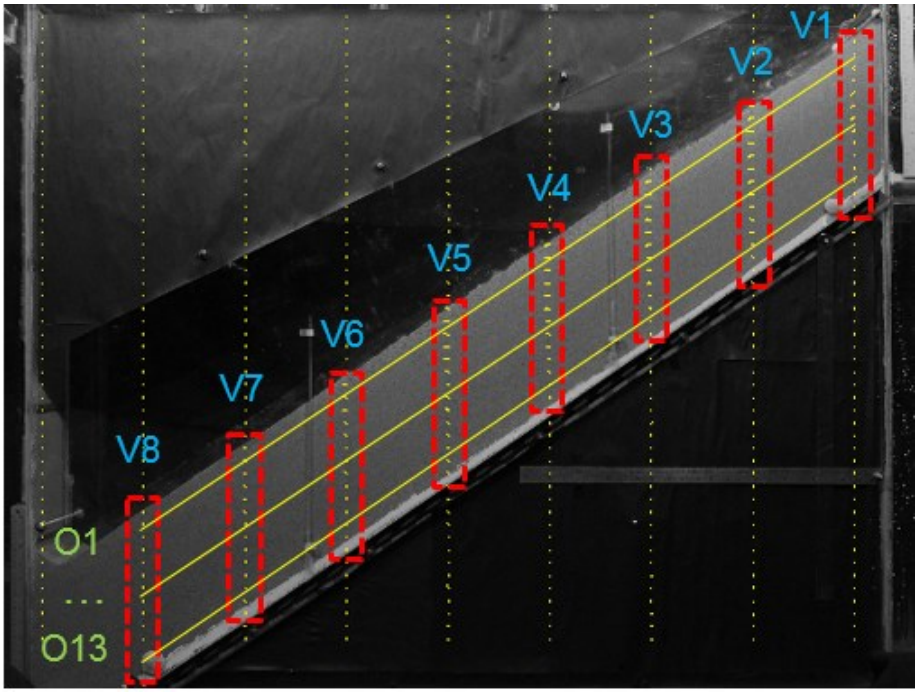

Figure 9. Locations of cross sections.

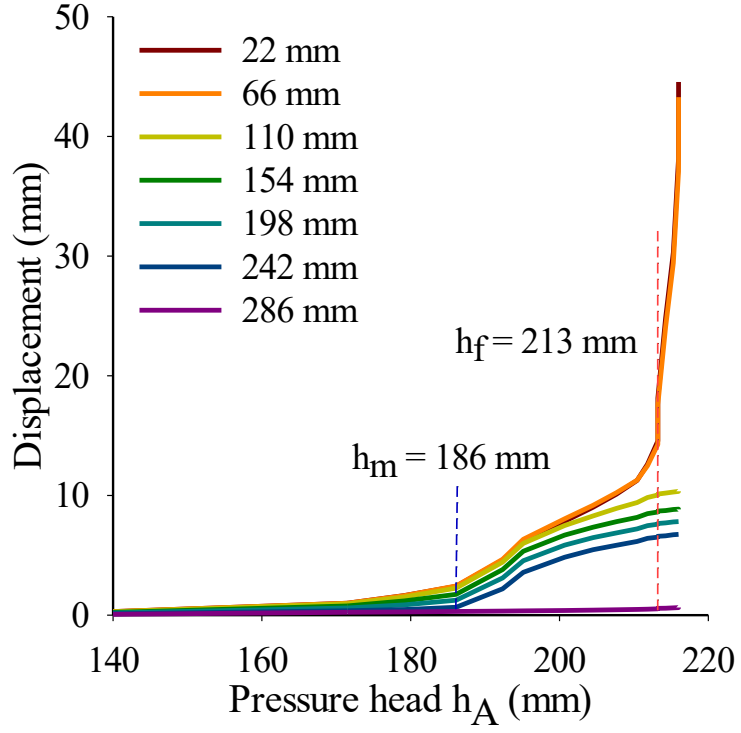

(a)

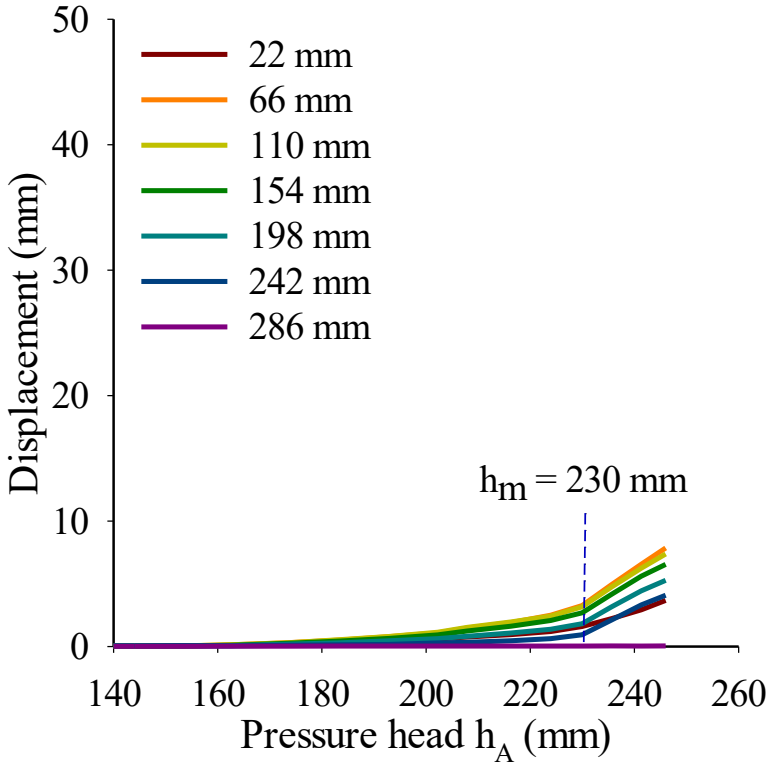

(b)

Figure 10. Displacement of soil at vertical cross section V3 versus upslope water pressure head (h_A): (a) without stabilisation; (b) with stabilisation.

542

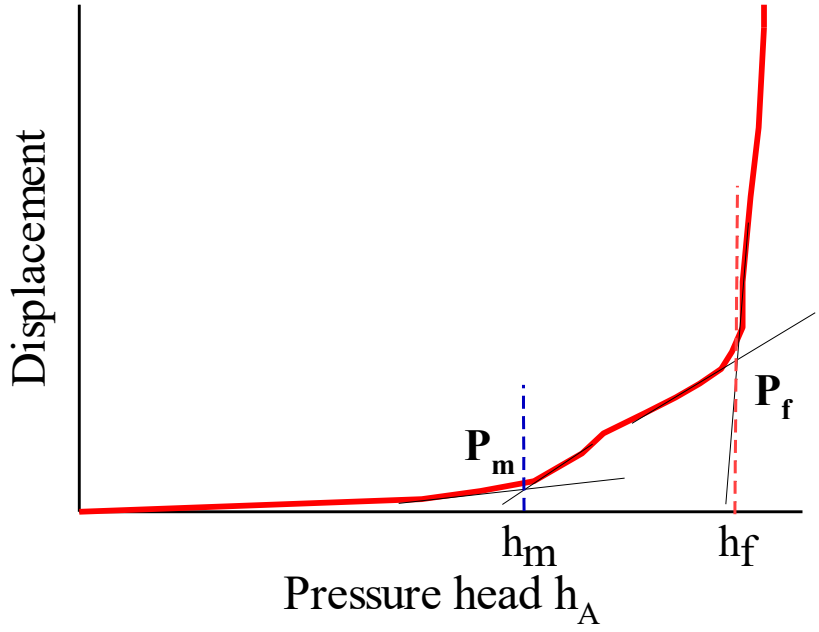

543

544 **Figure 11. Typical curve of displacement versus water pressure head h_A.**

545

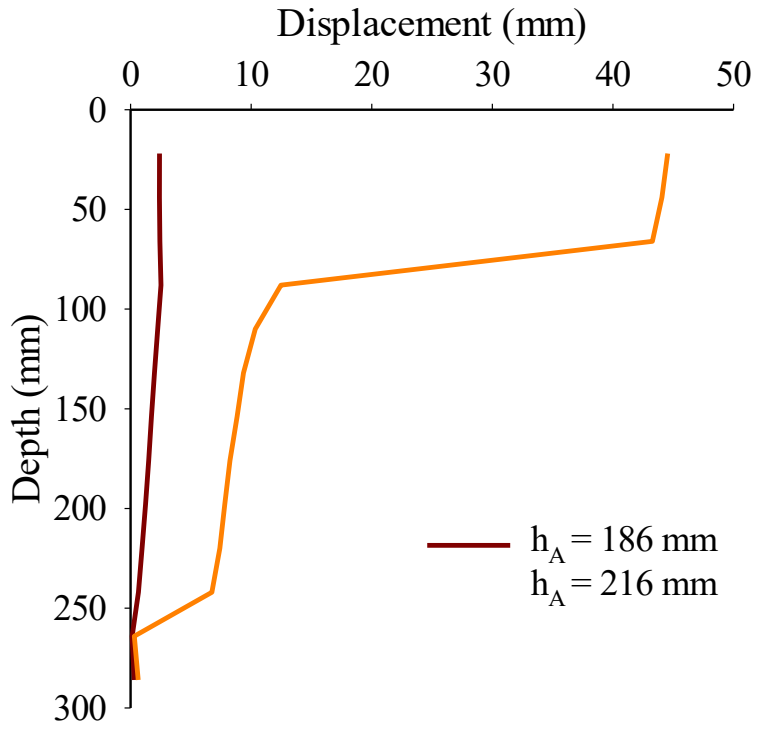

(a)

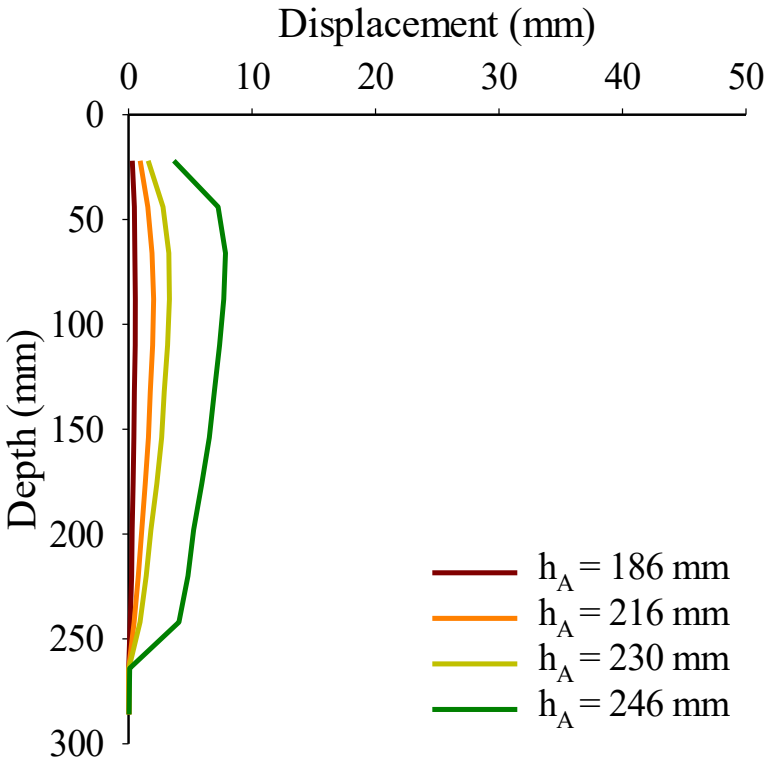

(b)

Figure 12. Variation of displacement with depth at section V3: (a) case 1: without stabilisation; (b) case 2: with stabilisation.

552

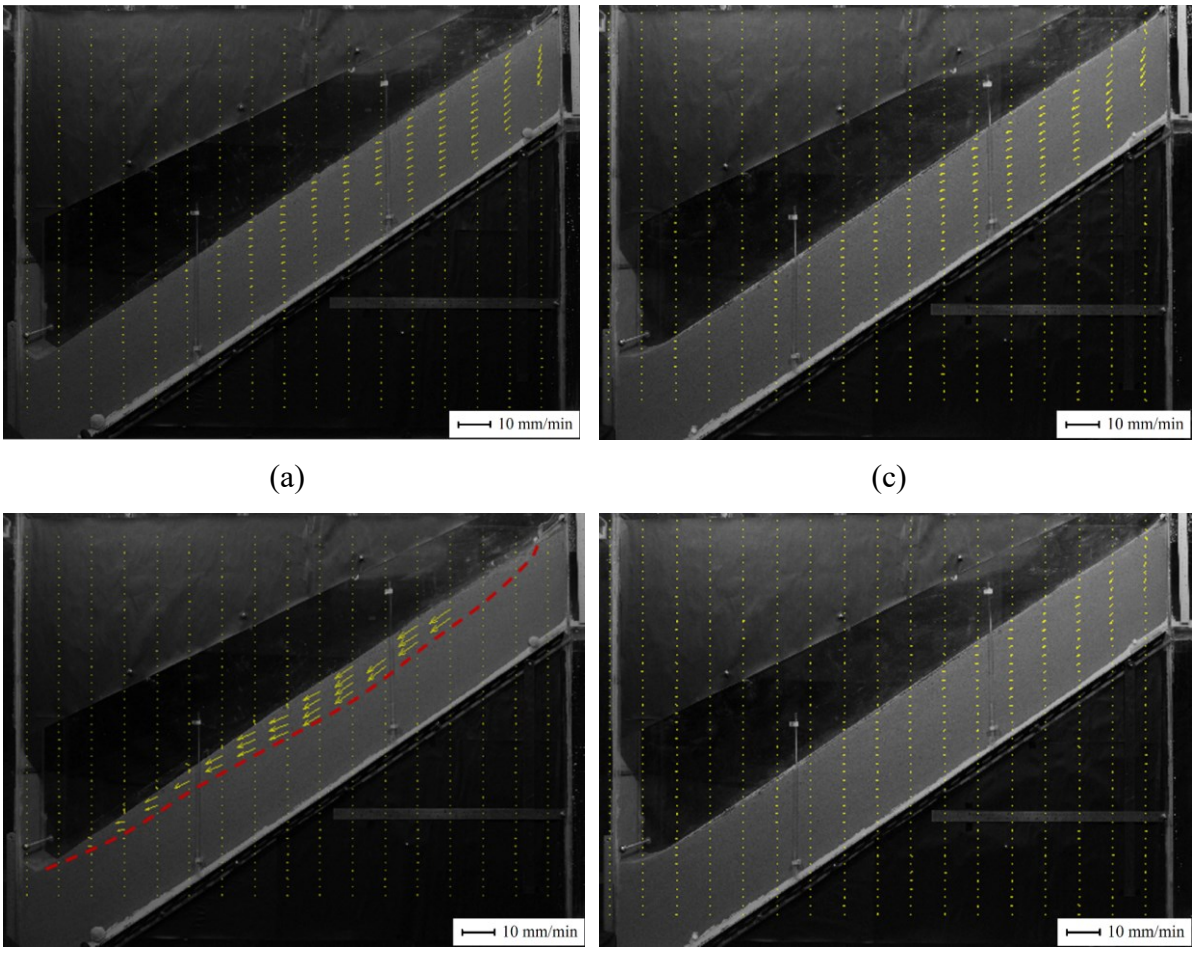

553 **Figure 13. Velocity vectors of soil particles: (a) case 1, h_A = 186 mm; (b) case 1,**
554 **h_A = 213 mm; (c) case 2, h_A = 230 mm; (d) case 2, h_A = 246 mm.**

555

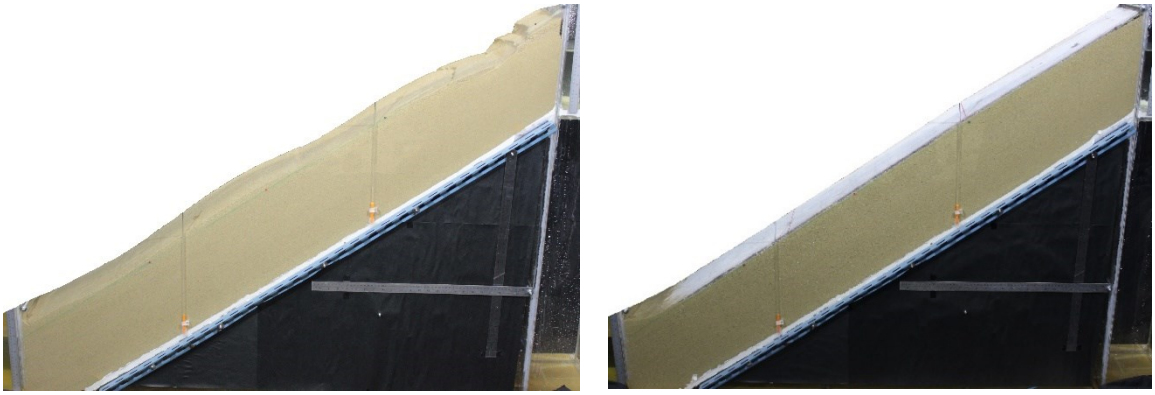

(a) (b)

Figure 14. Photographs of soil slope after test: (a) case 1: without stabilisation; (b) case 2: with stabilisation.

562 **List of Tables**
563
564
565
566
567
568
569

570 **Table 1. Properties of GCCM after being cured for 7 d [after Jongvivatsakul *et al.* (2018)]**
571

Property	GCCM	
	Width direction	Length direction
Nominal thickness [mm]	8.1	
Mass per unit area [g/cm^2]	1.35	
Tensile strength [kN/m]	26.5	16.3
Stiffness [MPa]	252.4	240.8
Bending strength [MPa]	9.9	6.6
Maximum puncture load [kN]	1.60	
Permeability [cm/s]	7.03×10^{-7}	

572
573

574 **Table 2. Physical and mechanical properties of sand**

Description	Value	Unit	Standard
Grain size distribution (sand:silt:clay)	100:0:0	%	ASTM D422
D_{10}	0.16	mm	-
D_{30}	0.19	mm	-
D_{60}	0.25	mm	-
Coefficient of uniformity, C_u	1.5	-	-
Coefficient of curvature, C_c	0.9	-	-
Classification	SP	-	ASTM D2487
Dry unit weight, γ_d	14.5	kN/m^3	ASTM D7263
Saturated unit weight, γ_{sat}	18.8	kN/m^3	-
Specific gravity, G_s	2.65	-	ASTM D854
Cohesion, c'	0	kPa	ASTM D3080
Angle of internal friction, ϕ	38	°	ASTM D3080
Hydraulic conductivity, k_{sat}	2.1×10^{-4}	m/s	ASTM D2434

575

576

577